

# Origin of p-Type Conduction in Amorphous CuI: A First-Principles Investigation

Miso Lee, Yong Youn, Jae Kyeong Jeong, Youngho Kang,\* and Seungwu Han\*

Recently, Jun et al. (*Adv. Mater.* 2018, 30, 1706573) reported Sn-doped amorphous phases of CuI (*a*-CuI) as a new class of transparent p-type semiconductors. It is surprising that high mobilities are found despite amorphous structures tend to localize carriers, particularly the directional p orbitals of anions. To reveal the microscopic origin of the new p-type amorphous semiconductors, density functional theory calculations are performed, and structural and electrical properties of *a*-CuI are investigated. Amorphous models from melt-quench simulations consist of structural motifs that resemble local orders in crystalline polymorphs of CuI. Despite the absence of translational symmetry, states at valence band maximum (VBM) are substantially extended in linear ways due to the hybridization between I-5p states, explaining the high hole mobilities in the experiment. Sn-doped *a*-CuI is also investigated and it is found that Sn atoms stabilize the amorphous structure without disturbing the hole transport. Furthermore, results on nonstoichiometric models show that Cu-deficiency increases the hole concentration in *a*-CuI and also enhances the delocalization of VBM states, which is consistent with the experimental observation that the hole mobility increases with doping concentrations. Herein, the origin of hole conduction in amorphous CuI is enlightened, which is believed to contribute in the development of high-performance p-type amorphous materials.

materials, amorphous oxide semiconductors (AOSs) like amorphous InGaZnO<sub>4</sub> have garnered great attention for electronics and energy applications due to superior film stability, high carrier mobility, and controllable doping concentrations.<sup>[4–6]</sup> Optical transparency over 80%, a result of wide band gaps (>3 eV), is another benefit of AOSs, enabling transparent electronics.<sup>[7–9]</sup>

P–n junctions are the crucial building blocks in many device architectures. However, current applications of AOSs are limited to unipolar devices because efficient AOSs usually exhibit n-type conductivity. Although p-type transport has been demonstrated with some crystalline oxides like SnO<sup>[10]</sup> and Cu<sub>2</sub>O,<sup>[11]</sup> their device properties are inferior to those of n-type oxides. For instance, the visible-light transparency and carrier mobility of n-type InGaZnO<sub>4</sub> are higher than 80% and 10 cm<sup>2</sup> V<sup>−1</sup> s<sup>−1</sup>,<sup>[12]</sup> respectively, whereas none of known p-type oxides achieved this level of transparency and carrier mobility simultaneously. More critically, these

p-type oxides lose the p-type character in amorphous phases.<sup>[13]</sup> As a result, high-performance p–n junctions comprising transparent amorphous semiconductors have not been realized yet. To overcome the current situation, potential wide bandgap p-type oxides were searched through high-throughput computational approaches,<sup>[14–17]</sup> but experimental verification is yet to follow.

Crystalline CuI with a zinc-blende structure ( $\gamma$ -CuI) is a promising transparent p-type semiconductor.<sup>[18,19]</sup> It is highly p-type dopable up to hole concentrations of 10<sup>19</sup> cm<sup>−3</sup> and transparent due to a wide bandgap of around 3.1 eV. In addition, single crystalline CuI shows high hole mobilities (>40 cm<sup>2</sup> V<sup>−1</sup> s<sup>−1</sup>). Researches on integrating CuI into actual devices are under way, and some experiments reported outstanding p-channel performance of CuI-based thin-film transistors.<sup>[20,21]</sup> Recently, Jun et al. demonstrated amorphous Sn-doped CuI (*a*-CuI:Sn) films can display high p-type conductivity while maintaining optical transparency at the level of crystalline CuI and structural stability of the amorphous phase at room temperature.<sup>[22]</sup> In particular, the hole mobilities of *a*-CuI:Sn were found to be 3–4 cm<sup>2</sup> V<sup>−1</sup> s<sup>−1</sup> by Hall measurements, which are comparable with those of polycrystalline CuI films.

Despite the great potential of *a*-CuI:Sn as a new class of transparent p-type semiconductors, the fundamental understanding of its structural and electrical properties is still incomplete.

## 1. Introduction

Amorphous materials (e.g., amorphous Si) have played an important role in electronic devices due to several technological merits such as low-cost and low-temperature processing, flexibility in the choice of substrates including plastics, and good uniformity of thin films.<sup>[1–3]</sup> Among various amorphous

M. Lee, Dr. Y. Youn, Prof. S. Han  
Department of Materials Science and Engineering  
Seoul National University  
Seoul 08826, Korea  
E-mail: hansw@snu.ac.kr

Prof. J. K. Jeong  
Department of Electronic Engineering  
Hanyang University  
Seoul 04763, Korea

Prof. Y. Kang  
Department of Materials Science and Engineering  
Incheon National University  
Incheon 22012, Korea  
E-mail: youngho84@inu.ac.kr

 The ORCID identification number(s) for the author(s) of this article can be found under <https://doi.org/10.1002/pssb.202000218>.

DOI: 10.1002/pssb.202000218

For instance, in AOSs, the conduction band is mainly composed of isotropic *s* orbitals of post-transition metals such that even without a long-range structural order, conduction paths can form for electrons via overlapping *s* orbitals.<sup>[4]</sup> However, I-5p and Cu-3d orbitals forming the valence band in *a*-CuI:Sn are highly directional unlike *s* orbitals. Therefore, the conduction mechanism of hole carriers in *a*-CuI:Sn is elusive, which can be an obstacle against further improving the electrical property of *a*-CuI:Sn.

Motivated by the earlier discussions, we investigate the physical properties of *a*-CuI:Sn using the density functional theory (DFT) calculations in this work. Amorphous structures are generated by molecular dynamics (MD) simulations and the local atomic configurations and electronic structures are analyzed. For simplicity, we first focus on *a*-CuI without Sn dopants because Sn dopants do not directly influence valence bands as will be revealed in a later section. We find that the coordination environment in *a*-CuI contains the structural characteristics of various CuI polymorphs. Analysis of electronic structures shows that the valence bands of *a*-CuI are fairly delocalized despite absence of long-range orders. This is due to substantial overlap between dispersive I-5p orbitals. Interestingly, 1D conduction channels develop for holes, which are attributed to antibonding I-5p orbitals. By examining *a*-CuI:Sn, we reveal that Sn primarily acts as a stabilizer of amorphous phases, but rarely affects the hole conduction pathway. Nonstoichiometric *a*-CuI:Sn (*a*-Cu<sub>1-x</sub>I:Sn) is also studied, which shows that Cu deficiency increases the hole concentration in *a*-CuI and also enhances the delocalization of the valence band maximum (VBM) state.

## 2. Methods

The first-principles calculations were carried out using the Vienna *ab initio* simulation package (VASP) with projector-augmented waves (PAWs) for MD simulation and electronic structure calculations.<sup>[23,24]</sup> The Perdew–Burke–Ernzerhof (PBE) functional was used for the exchange–correlation energy of electrons.<sup>[25]</sup> For a better description of the strongly localized Cu-3d orbitals, we applied the onsite Coulomb energy (*U*) of 4 eV on Cu-3d states.<sup>[26]</sup> Applying *U* lowers occupied Cu-3d levels, yielding the shape and peak structure of Cu-3d states of  $\gamma$ -CuI comparable with the results from X-ray photoemission spectroscopy (Figure S1a, Supporting Information).<sup>[27–29]</sup> We do not consider *U* for Sn because Sn-4d states lie deep in energy. The energy cutoff for the plane-wave basis was chosen to be 300 eV. For the *k*-point sampling, we selected only the  $\Gamma$  point for MD and structural optimization, whereas the  $3 \times 3 \times 3$  Monkhorst–Pack grid was used in investigating electronic structures. In PBE + *U* calculations, the bandgap still underestimated experimental data. To address this, we compared the PBE + *U* results with more accurate hybrid functional calculations. In the hybrid calculations,<sup>[30]</sup> we used 32% of Fock exchange energy, which produced a bandgap (2.97 eV) in good agreement with experiments (2.98 eV). For  $\gamma$ -CuI, we confirmed that PBE + *U* produced valence bands that were comparable with those of hybrid functional (Figure S1b, Supporting Information).

Amorphous structures were generated using the melt-quench method with a canonical ensemble. Atomic positions were initialized by randomly distributing atoms in cubic supercells.

The structures were then melted for 10 ps at 1200 K that was slightly higher than the experimental melting point of CuI (879 K). This temperature was enough to melt the structure (see the ion-averaged mean square displacement of Cu and I in Figure S2, Supporting Information). Afterward, the structures were cooled down to 300 K with  $-100 \text{ K ps}^{-1}$  rate. A slower cooling rate ( $-50 \text{ K ps}^{-1}$ ) did not cause any meaningful variation in the atomic structures (Figure S3, Supporting Information). Finally, we obtained amorphous models by relaxing the structures until atomic forces became less than  $0.02 \text{ eV \AA}^{-1}$ . As the doping ratio of Sn in the synthesized *a*-CuI:Sn film was not clearly stated, we set the ratio of  $N_{\text{Sn}}/(N_{\text{Cu}} + N_{\text{Sn}})$  to 5.3% that was close to the molar ratio in precursor solutions used in experiments.<sup>[22]</sup> We focused on Sn<sup>2+</sup> for the charge state of Sn, but considering Sn<sup>4+</sup> did not affect our conclusions (Figure S4, Supporting Information). For *a*-Cu<sub>1-x</sub>I:Sn models, we used  $x = 0.014$  and  $0.028$ , which were the lowest and second lowest numbers, respectively, which can be considered in this work for *x* within the given supercells. Although the Cu deficiency was not reported quantitatively in the study by Jun et al.,<sup>[22]</sup> these *x* values correspond to the Cu vacancy concentration of  $1\text{--}4 \times 10^{20} \text{ cm}^{-3}$  found in CuI films.<sup>[31]</sup> The number of atoms with type *i* ( $N_i$ ) considered in this work are shown in Table 1. Every defect (Sn dopants and Cu vacancy) was introduced before the melt, which allowed us to identify defect configurations without any bias, in contrast to a method that introduced defects after the melt-quench process.<sup>[32]</sup>

For the initial mass density in the MD simulations, because the experimental density was not available for *a*-CuI, we examined several values between  $4.44$  and  $5.48 \text{ g cm}^{-3}$ , which corresponds to 80% and 98% of the density of  $\gamma$ -CuI, respectively. This range was determined by considering the density difference between the amorphous and crystalline phases found in other amorphous materials (e.g., the reported density ratio of the amorphous materials with respect to the crystalline counterpart was 98% for Si, 83% and SiO<sub>2</sub>, 18–23% for Al<sub>2</sub>O<sub>3</sub>, and 4–11% for ZnO).<sup>[33–35]</sup> Herein, we focused on the results obtained using  $4.44 \text{ g cm}^{-3}$  as the initial mass density, but the structural and electronic characteristics and total energies barely depended on the initial mass density (Figure S5 and S6, Supporting Information). For considering structural fluctuations in the amorphous phase, three models of each system shown in Table 1 are built independently. The average total energies of the *a*-CuI structures were  $\approx 40 \text{ meV atom}^{-1}$  higher than that of  $\gamma$ -CuI, which was smaller than for other amorphous materials.<sup>[33,35,36]</sup> The smaller excess energy in *a*-CuI would stem from the flexible coordination environment in *a*-CuI, as inferred by the presence of various crystal polymorphs with similar

**Table 1.** Summary of the number of atoms in the amorphous models considered in this work.

	<i>a</i> -CuI	<i>a</i> -CuI:Sn	<i>a</i> -Cu <sub>1-x</sub> I:Sn	
			$x = 0.014$	$x = 0.028$
$N_{\text{Cu}}$	72	72	71	70
$N_{\text{Sn}}$	0	4	4	4
$N_{\text{I}}$	72	80	80	80

energies but different local environments (see the following paragraphs).

### 3. Results and Discussion

#### 3.1. Structural Properties

We show the crystal structure of  $\gamma$ -CuI and a typical structure of  $\alpha$ -CuI in **Figures 1a,b**, respectively. In  $\gamma$ -CuI, both Cu and I ions are tetrahedrally coordinated by the other ion. This local coordination motif in  $\gamma$ -CuI is not strictly preserved in  $\alpha$ -CuI. Instead, the atomic structure of  $\alpha$ -CuI includes structural characteristics from various polymorphs with different local environments (detailed information on five polymorphs found in experiments are shown in **Table 2**<sup>[37–40]</sup> and their atomic structures and local coordination environments are shown in Figure S7, Supporting Information). For example, the coordination number (CN) of ions fluctuates between 3 and 4 in the amorphous phase, which leads to the averaged CN smaller than 4. Furthermore, the

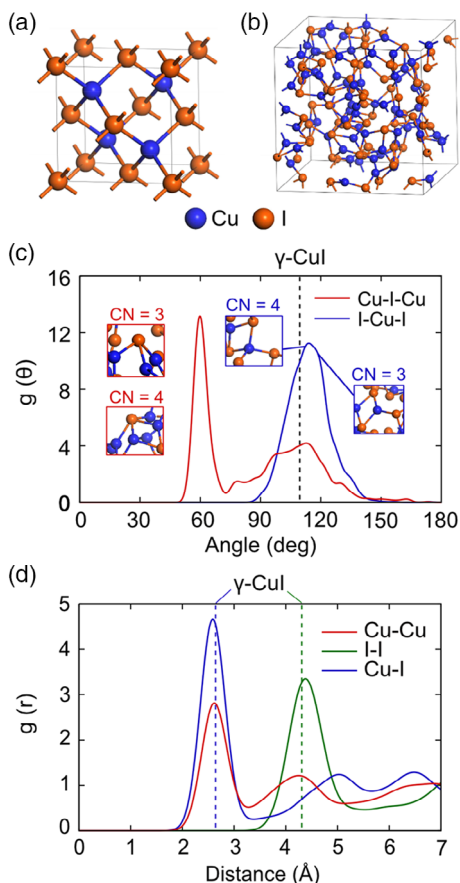


**Figure 1.** Atomic structures of a)  $\gamma$ -CuI and b)  $\alpha$ -CuI. c) Ion-averaged angle distribution functions (ADFs) for Cu–I–Cu and I–Cu–I in  $\alpha$ -CuI. The representative local structures depending on CN are shown in the insets. d) Ion-averaged RDFs for Cu–Cu, I–I, and Cu–I in  $\alpha$ -CuI. ADFs and RDFs are averaged over three different structures. Corresponding bond angle and distances between nearest neighbors for  $\gamma$ -CuI are marked as vertical dashed lines in (c) and (d), respectively. In  $\gamma$ -CuI, the Cu–Cu and I–I distances are the same.

**Table 2.** Crystal system, space group, relative energy, and nearest neighbor distance for various CuI polymorphs.

Crystal system	Space group	Relative energy [meV atom <sup>−1</sup> ]	Nearest neighbor distance [Å]	
			Cu–I	Cu–Cu
Cubic <sup>[37]</sup>	$F\bar{4}3m$	0	2.64	4.31
Tetragonal <sup>[38]</sup>	$P4/nmm$	5	2.67	2.94
Hexagonal <sup>[39]</sup>	$P6_3mc$	9	2.64	4.32
Trigonal <sup>[40]</sup>	$P3m1$	13	2.63	2.87
Orthorhombic <sup>[38]</sup>	$Cmcm$	73	2.59	2.51

diverse forms of local geometries in addition to the tetrahedral shape occur in  $\alpha$ -CuI, as evidenced by the large difference of bond angles from 109.5° (see the angle distribution functions [ADFs] for Cu–I–Cu and I–Cu–I in Figure 1c that are averaged over ions). To be specific, we identify two representative local orders for I and Cu, as shown in the insets of Figure 1c. First, fourfold I ions dominantly form pyramidal structures rather than tetrahedral ones. This type of local order is discovered in the tetragonal phase of CuI. In contrast, threefold I ions mostly exhibit trigonal pyramidal shapes like ammonia molecules, which has no corresponding local order in crystalline phases. Unique local orders of amorphous phases were also reported for other materials.<sup>[35,36,41]</sup> These I-centered motifs produce two distinct Cu–I–Cu bond angles around 60° and 100°, as found in the tetragonal phase. On the other hand, Cu ions with CN = 4 maintain the tetrahedral shape. When Cu ions have threefold coordinations, they exist in a form of trigonal planar geometry, yielding bond angles of 120° for I–Cu–I, like Cu ions in the orthorhombic phase.

Figure 1d shows ion-averaged radial distribution functions (RDFs) for Cu–I, Cu–Cu, and I–I. The averaged Cu–I bond length indicated by the first peak position is very close to those of the crystalline phases (Table 2). This agreement means that the ionic character of Cu–I bonds is well conserved in  $\alpha$ -CuI. Consistently, the ion-averaged charges of Cu and I obtained by the Bader analysis<sup>[42]</sup> are the same in  $\gamma$ -CuI and  $\alpha$ -CuI within 0.1%. In contrast, it is seen in the Cu–Cu RDF that some of Cu pairs have the distance of 2.65 Å. This Cu–Cu distance is far smaller than that in  $\gamma$ -CuI (4.31 Å), but similar distances are found in other polymorphs such as the tetragonal, trigonal, and orthorhombic phases (Table 2). Such a short distance between Cu ions can occur because of disperse I-5p states that effectively screen repulsive interactions between cations. Conversely, the large size of I-5p states prevents I ions from being too close to each other in  $\alpha$ -CuI, as happened to crystalline phases. We note that the short Cu–Cu distances in  $\alpha$ -CuI do not imply the precipitation of pure Cu phases because the Cu ions form chemical bonds mainly with I ions and pure Cu regions do not exist (Figure S8, Supporting Information).

#### 3.2. Electronic Properties

Next, we analyze the electronic structure to investigate the carrier transport. It is known that the degree of the localization of

electronic states in disordered systems is critically affected by the size and directionality of contributing atomic orbitals.<sup>[43]</sup> **Figure 2a** shows orbital-resolved partial density of states (PDOSs) averaged over three *a*-CuI models (similar electronic structures are commonly found in all *a*-CuI models examined in this study, as shown in Figure S9, Supporting Information). We see that the lowest parts of the conduction bands are mainly derived by Cu-4s and I-5s states with minor contributions of I-5p and Cu-3d states. Due to the spherical symmetry of s states, the conduction bands are spread over many atomic sites despite the absence of long-range ordering in the atomic arrangement, as shown in the charge density distribution for the conduction band minimum (CBM) in Figure 2b. We confirm this quantitatively by evaluating the inverse participation ratio (IPR) defined as

$$\text{IPR} = \frac{\sum_i^N w_i^2}{(\sum_i^N w_i)^2} \quad (1)$$

where  $N$  is the total number of the atoms in the supercell and  $w_i$  is the partial weight on the  $i$ th atom for a given state. IPR is  $1/N$  if the state is evenly distributed over every atom, whereas it becomes unity when it is localized at a single atomic site. Thus, IPR is a measure of the degree of localization of a given electronic state. Although the IPRs are slightly pronounced near the conduction band edge, they are mostly less than 0.1 (Figure 2a).

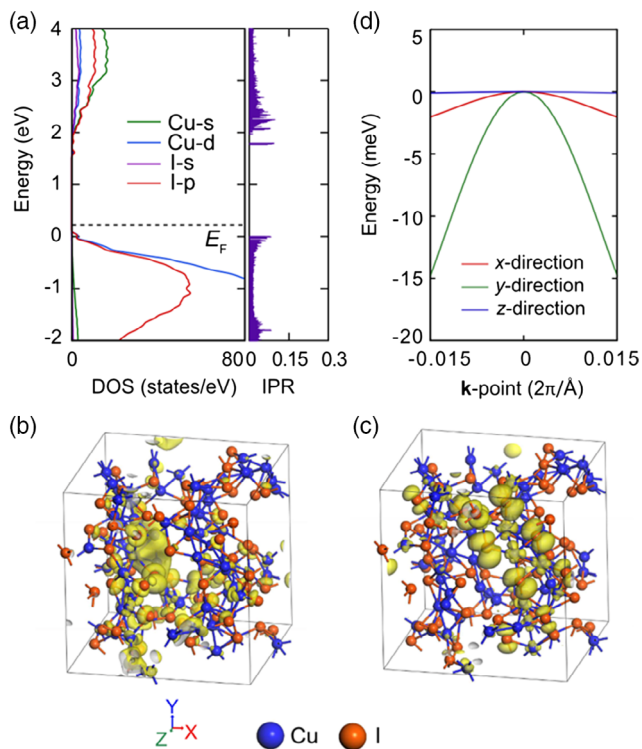


**Figure 2.** a) Supercell-averaged PDOS and IPR for *a*-CuI. The VBM is set to zero. The Fermi level ( $E_F$ ) is marked as a dashed line. The charge density distribution of the b) CBM and c) VBM. Isosurface values are set to 0.0003 and 0.001  $e \text{ bohr}^{-3}$  in (b) and (c), respectively. d) Band dispersion of the VBM along the  $x$ ,  $y$ , and  $z$  directions in the reciprocal space. The VBM is set to zero.

We find that the valence bands mainly consist of Cu-3d and I-5p states. One may expect a strong localization due to directionality of d and p orbitals. Indeed, the valence bands of AOSs like  $\text{InGaZnO}_4$  and ZnO and thermal oxides like  $\text{Al}_2\text{O}_3$  dominated by O-2p states are highly localized over a few oxygen sites (two O atoms in extreme cases).<sup>[44–46]</sup> Interestingly, however, the localization of valence states is much weaker in *a*-CuI compared with AOSs; the charge density of the VBM is distributed over multiple atomic sites (Figure 2c), yielding small IPR values below 0.1 (Figure 2a). The same delocalization features of both the conduction and valence bands also appear in bandgap-corrected hybrid calculations for the same structure (Figure S10, Supporting Information).

The weak localization of valence bands in *a*-CuI can be understood by hybridization between dispersive I-5p states, as pointed out in the study by Jun et al.<sup>[22]</sup> In particular, we notice that the I-5p orbitals at the VBM are aligned in a certain direction, producing a 1D conduction path. Such linear networking arises from antibonding characters of I-5p orbitals at the valence bands; the I-5p orbitals point to each other and form continuous  $\text{pp}\pi^*$  bonding, which maximizes the orbital hybridization and develops antibonding states around the VBM. We also find that Cu-3d states play a role in the delocalization of the VBM because they have similar energies with I-5p states. We corroborate this by replacing Cu (ionic radius of 0.77 Å) with Li (ionic radius of 0.76 Å) without further relaxation; the VBM somewhat loses the connectivity of the charge density distribution when Cu is replaced by Li (**Figure 3a**). As a result, the IPRs for states near the VBM in amorphous LiI (*a*-LiI) increase to 0.2, more than twice those in *a*-CuI (Figure 3b). The importance of the interaction between first-nearest neighbors was also shown for AOSs in a previous study.<sup>[47]</sup> By virtue of the effective networking of atomic states of the VBM along a certain direction, a moderate energy dispersion, i.e., small effective masses, appears only for the corresponding direction (the  $\Gamma$ -Y direction in Figure 2d). (The degree of band dispersion slightly differs among different supercells, as shown in Figure S11, Supporting Information.) In real materials, such 1D conduction paths will form in various directions and link to each other, enabling 3D flow of hole carriers. These calculation results show why *a*-CuI can exhibit high

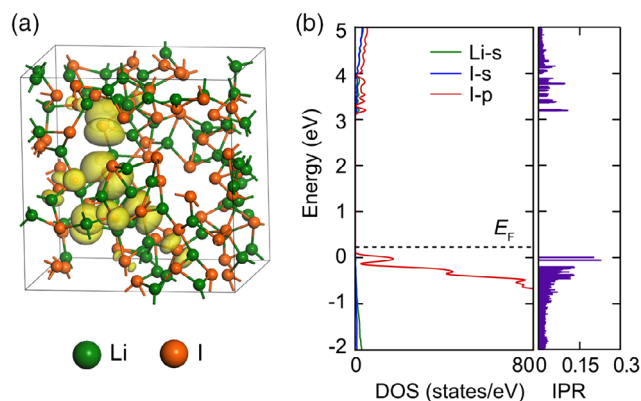


**Figure 3.** a) Atomic structure and charge density distribution of the VBM and b) PDOS and IPR for *a*-LiI. The VBM is set to 0. The Fermi level ( $E_F$ ) is marked as a dashed line.

hole mobilities in spite of structural disorders. Regarding the transport mechanism, in light of the delocalization of the valence bands as well as the positive dependence of the hole mobility on the carrier concentration in experiments,<sup>[22]</sup> hole conduction would occur via the percolation process<sup>[48]</sup> or band transport with significant scattering arising from potential fluctuations.<sup>[49]</sup>

The bandgap is also of interest for *a*-CuI because it determines the optical transparency. According to a previous study on In-based AOSs,<sup>[44]</sup> the conduction bands gravitate toward lower energies because under-coordinated In ions are electrostatically more stable. As a result, optical bandgaps of amorphous phases are smaller than for its crystalline counterpart by 0.7 eV. Furthermore, long valence band tails in those materials cause the onset of absorption to further shift to lower energy by 0.55 eV, undermining the transparency. In *a*-CuI, however, such a significant bandgap narrowing is unlikely to happen because of uniform reduction in CNs of Cu and I ions as well as negligible tail states (Figure 2a). We indeed find that *a*-CuI has bandgaps slightly higher than  $\gamma$ -CuI by less than 0.2 eV, which is consistent with the experiment.<sup>[22]</sup>

### 3.3. Influence of Sn Doping and Cu Deficiency

From the analysis of atomic structures of *a*-CuI:Sn (Figure 4a), we find that Sn ions are bonded with three to five I ions within the first coordination shell (see red dashed circles), but they do not alter the local structures of Cu and I compared with *a*-CuI. Regarding the electronic structure, Sn-5p orbitals develop empty states near the conduction band bottom (Figure 4b) by hybridizing with neighboring I-5p orbitals. These states are fairly localized, as evidenced by the large IPR values (0.1–0.3). Meanwhile, Sn doping barely affects the valence bands that remain delocalized in *a*-CuI:Sn as in *a*-CuI (Figure 4b). Overall, our results show that the main role played by Sn in *a*-CuI is to stabilize the amorphous structure, not hampering the hole conduction, as suggested in the study by Jun et al.<sup>[22]</sup>

In  $\gamma$ -CuI, Cu vacancies are known to be the source of hole carriers.<sup>[50]</sup> Similarly, we also find that Cu deficiency in the amorphous phase can contribute to hole doping: the Fermi level

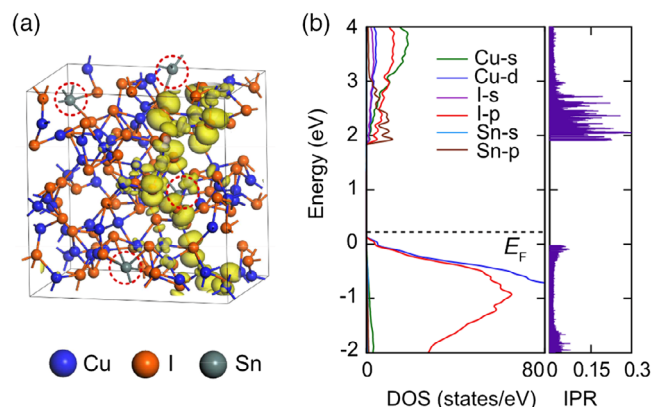


**Figure 4.** a) Atomic structure and charge density distribution of the VBM for *a*-CuI:Sn. Red dashed circles indicate the positions of Sn ions. b) Supercell-averaged PDOS and IPR for *a*-CuI:Sn. The VBM is set to 0. The Fermi level ( $E_F$ ) is marked as a dashed line.

in *a*-Cu<sub>1-x</sub>I:Sn lies below the VBM without creating deep levels inside the gap, as shown in PDOSs for  $x = 0.014$  (Figure 5a) and 0.028 (Figure 5b). It is intriguing to note that the degree of delocalization of the valence bands becomes enhanced with increasing Cu deficiency, as shown in the charge distribution of the VBM in Figure 6. This is also confirmed by a decrease in the sample-averaged IPR values from stoichiometric *a*-CuI:Sn (0.0467) to nonstoichiometric *a*-Cu<sub>1-x</sub>I:Sn with  $x = 0.014$  (0.03) and 0.028 (0.021). The enhanced delocalization may occur due to the following reason: once holes that are created by the lack of

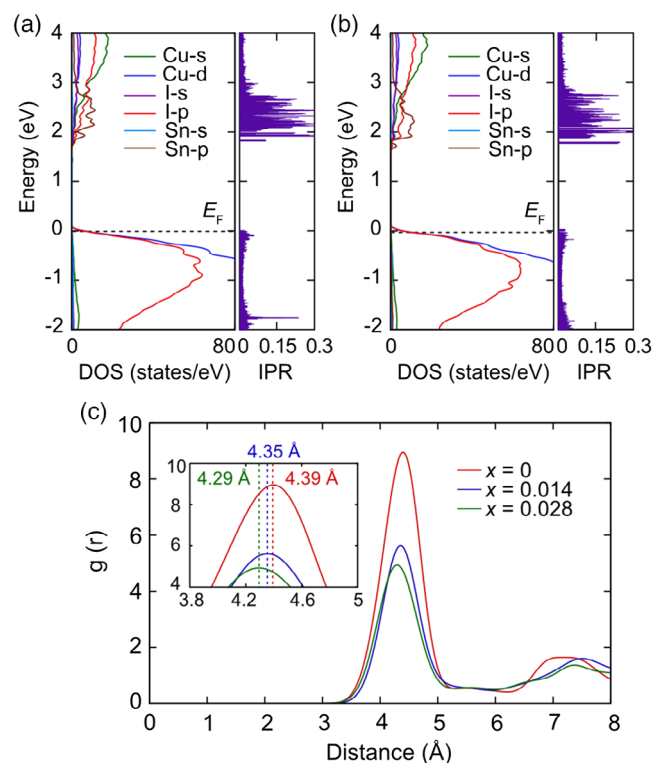


**Figure 5.** Supercell-averaged PDOS and IPR for *a*-Cu<sub>1-x</sub>I:Sn with a)  $x = 0.014$  and b)  $x = 0.028$ . The VBM is set to 0. The Fermi level ( $E_F$ ) is marked as a dashed line. c) Ion-averaged I-I RDFs for *a*-Cu<sub>1-x</sub>I:Sn with  $x = 0, 0.014$ , and  $0.028$ . In the inset, the RDFs are zoomed-in near the first peak positions.

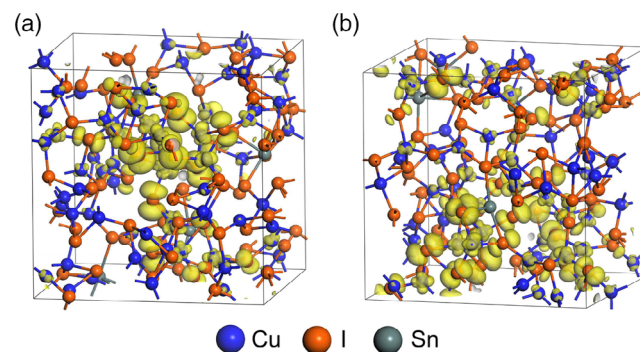


**Figure 6.** Atomic structure and charge density distribution of the VBM of *a*-Cu<sub>1-x</sub>I:Sn with a)  $x = 0.014$  and b)  $0.028$ .

Cu ions occupy the valence bands, I ions get closer to each other because the antibonding states become empty, as shown in the RDFs for I–I in Figure 5c (in this figure, we focus on I ions with  $w_i$  for the VBM higher than 0.005). Consequently, hybridization between I-5p states strengthens, leading to more extended valence states. In particular, short distances among I ions spread the valence states further around one-dimensional paths, as shown in the charge distribution of the VBM for  $a$ -Cu $_{1-x}$ I:Sn with  $x = 0.014$  and  $x = 0.028$  in Figures 6a,b, respectively. This would explain why the hole mobility increases with the carrier density in experiments.<sup>[22]</sup>

## 4. Conclusions

In summary, we carried out first-principles calculations to investigate the structural and electronic properties of amorphous CuI. We found that the local Cu–I coordination motifs in  $a$ -CuI include structural features of diverse crystalline CuI polymorphs. Despite the lack of long-range orders in the amorphous structure, the valence bands remain to be fairly delocalized, particularly along a certain direction, because of the antibonding interaction between dispersive I-5p states. The present finding elucidates why  $a$ -CuI behaves as good p-type conductors in spite of structural disorder. Our results for  $a$ -CuI:Sn revealed that the structural and electronic characteristics of  $a$ -CuI rarely change on Sn doping. As a result, the role of Sn in  $a$ -CuI is limited to the stabilizer of the amorphous structure. (The suppressed crystallization of  $a$ -CuI:Sn would be attributed to the different valences of Sn (Sn<sup>2+</sup> or Sn<sup>4+</sup>) from that of Cu<sup>1+</sup>[22]). We also demonstrated that Cu deficiency generates holes in  $a$ -CuI, which in turn enhances the degree of delocalization of the valence bands. This result would explain the reason for the increase in the mobility with the hole concentration. By providing important insights into the physical properties of  $a$ -CuI, we believe that this work will help design new wide bandgap p-type semiconductors.

## Supporting Information

Supporting Information is available from the Wiley Online Library or from the author.

## Acknowledgements

M.L. and Y.Y. contributed equally to this work. This work was supported by Samsung Research Funding Center for Future Technology through Samsung Electronics. The computations were carried out at the KISTI supercomputing center (KSC-2019-CRE-0131).

## Conflict of Interest

The authors declare no conflict of interest.

## Keywords

amorphous p-type semiconductors, cuprous iodide, density functional theory, high mobilities

Received: April 16, 2020  
Revised: May 20, 2020  
Published online: June 23, 2020

- [1] W. E. Spear, P. G. Le Comber, *Solid State Commun.* **1975**, *17*, 1193.
- [2] M. J. Powell, *IEEE Trans. Electron Devices* **1989**, *36*, 2753.
- [3] P. G. le Comber, W. E. Spear, A. Ghaith, *Electron. Lett.* **1979**, *15*, 179.
- [4] K. Nomura, H. Ohta, A. Takagi, T. Kamiya, M. Hirano, H. Hosono, *Nature* **2004**, *432*, 488.
- [5] H. Kumomi, K. Nomura, T. Kamiya, H. Hosono, *Thin Solid Films* **2008**, *516*, 1516.
- [6] T. Kamiya, K. Nomura, H. Hosono, *Sci. Technol. Adv. Mater.* **2010**, *11*, 044305.
- [7] E. Fortunato, P. Barquinha, R. Martins, *Adv. Mater.* **2012**, *24*, 2945.
- [8] M. Lorenz, M. S. Ramachandra Rao, T. Venkatesan, E. Fortunato, P. Barquinha, R. Branquinho, D. Salgueiro, R. Martins, E. Carlos, A. Liu, F. K. Shan, M. Grundmann, H. Boschker, J. Mukherjee, M. Priyadarshini, N. DasGupta, D. J. Rogers, F. H. Teherani, E. V. Sandana, P. Bove, K. Rietwyk, A. Zaban, A. Veziridis, A. Weidenkaff, M. Muralidhar, M. Murakami, S. Abel, J. Fompeyrine, J. Zuniga-Perez, R. Ramesh et al., *J. Phys. Appl. Phys.* **2016**, *49*, 433001.
- [9] K. Ide, K. Nomura, H. Hosono, T. Kamiya, *Phys. Status Solidi A* **2019**, *216*, 1800372.
- [10] J. A. Caraveo-Frescas, P. K. Nayak, H. A. Al-Jawhari, D. B. Granato, U. Schwingenschlögl, H. N. Alshareef, *ACS Nano* **2013**, *7*, 5160.
- [11] H. Nagai, T. Suzuki, H. Hara, C. Mochizuki, I. Takano, T. Honda, M. Sato, *Mater. Chem. Phys.* **2012**, *137*, 252.
- [12] A. Suresh, P. Wellenius, A. Dhawan, J. Muth, *Appl. Phys. Lett.* **2007**, *90*, 123512.
- [13] S. Narushima, H. Mizoguchi, K. Shimizu, K. Ueda, H. Ohta, M. Hirano, T. Kamiya, H. Hosono, *Adv. Mater.* **2003**, *15*, 1409.
- [14] G. Hautier, A. Miglio, G. Ceder, G.-M. Rignanese, X. Gonze, *Nat. Commun.* **2013**, *4*, 2292.
- [15] N. Sarmadian, R. Saniz, B. Partoens, D. Lamoen, *Sci. Rep.* **2016**, *6*, 20446.
- [16] K. Yim, Y. Youn, M. Lee, D. Yoo, J. Lee, S. H. Cho, S. Han, *NPJ Comput. Mater.* **2018**, *4*, 1.
- [17] Y. Youn, M. Lee, D. Kim, J. K. Jeong, Y. Kang, S. Han, *Chem. Mater.* **2019**, *31*, 5475.
- [18] D. Chen, Y. Wang, Z. Lin, J. Huang, X. Chen, D. Pan, F. Huang, *Cryst. Growth Des.* **2010**, *10*, 2057.
- [19] J. Wang, J. Li, S.-S. Li, *J. Appl. Phys.* **2011**, *110*, 054907.
- [20] C.-H. Choi, J. Y. Gorecki, Z. Fang, M. Allen, S. Li, L.-Y. Lin, C.-C. Cheng, C.-H. Chang, *J. Mater. Chem. C* **2016**, *4*, 10309.
- [21] A. Liu, H. Zhu, W.-T. Park, S.-J. Kang, Y. Xu, M.-G. Kim, Y.-Y. Noh, *Adv. Mater.* **2018**, *30*, 1802379.
- [22] T. Jun, J. Kim, M. Sasase, H. Hosono, *Adv. Mater.* **2018**, *30*, 1706573.
- [23] G. Kresse, J. Furthmüller, *Phys. Rev. B* **1996**, *54*, 11169.
- [24] G. Kresse, J. Hafner, *Phys. Rev. B* **1993**, *47*, 558.
- [25] J. P. Perdew, K. Burke, M. Ernzerhof, *Phys. Rev. Lett.* **1996**, *77*, 3865.
- [26] L. Wang, T. Maxisch, G. Ceder, *Phys. Rev. B* **2006**, *73*, 195107.
- [27] A. Goldmann, J. Tejada, N. J. Shevchik, M. Cardona, *Phys. Rev. B* **1974**, *10*, 4388.
- [28] J. G. Gross, M. Fliyou, S. Lewonczuk, J. Ringeissen, R. Pinchaux, *Phys. Rev. B* **1988**, *37*, 3068.
- [29] A. V. Generalov, A. S. Vinogradov, *Phys. Solid State* **2013**, *55*, 1136.
- [30] J. Heyd, G. E. Scuseria, M. Ernzerhof, *J. Chem. Phys.* **2003**, *118*, 8207.
- [31] J. Coroa, B. M. Morais Faustino, A. Marques, C. Bianchi, T. Koskinen, T. Juntunen, I. Tittonen, I. Ferreira, *RSC Adv.* **2019**, *9*, 35384.
- [32] H. Song, G. Kang, Y. Kang, S. Han, *Phys. Status Solidi B* **2019**, *256*, 1800486.

- [33] Y. Youn, Y. Kang, S. Han, *Comput. Mater. Sci.* **2014**, *95*, 256.
- [34] J. Strand, O. A. Dicks, M. Kaviani, A. L. Shluger, *Microelectron. Eng.* **2017**, *178*, 235.
- [35] D. Mora-Fonz, A. L. Shluger, *Phys. Rev. B* **2019**, *99*, 014202.
- [36] A. Walsh, J. L. F. Da Silva, S.-H. Wei, *Chem. Mater.* **2009**, *21*, 5119.
- [37] D. A. Keen, S. Hull, *J. Phys.: Condens. Matter* **1995**, *7*, 5793.
- [38] M. Hofmann, S. Hull, D. A. Keen, *Phys. Rev. B* **1995**, *51*, 12022.
- [39] S. Miyake, S. Hoshino, T. Takenaka, *J. Phys. Soc. Jpn.* **1952**, *7*, 19.
- [40] R. Kurdyumova, R. Baranova, *Kristallografiya* **1961**, *6*, 402.
- [41] G. Kang, D. Lee, K. Lee, J. Kim, S. Han, *Phys. Rev. Appl.* **2018**, *10*, 064052.
- [42] G. Henkelman, A. Arnaldsson, H. Jónsson, *Comput. Mater. Sci.* **2006**, *36*, 354.
- [43] H. Hosono, *J. Non-Cryst. Solids* **2006**, *352*, 851.
- [44] Y. Kang, H. Song, H.-H. Nahm, S. H. Jeon, Y. Cho, S. Han, *APL Mater.* **2014**, *2*, 032108.
- [45] D. Mora-Fonz, A. L. Shluger, *Adv. Electron. Mater.* **2020**, *6*, 1900760.
- [46] O. A. Dicks, A. L. Shluger, *J. Phys.: Condens. Matter* **2017**, *29*, 314005.
- [47] Y. Kang, S. H. Jeon, Y.-W. Son, Y.-S. Lee, M. Ryu, S. Lee, S. Han, *Phys. Rev. Lett.* **2012**, *108*, 196404.
- [48] K. Nomura, T. Kamiya, H. Ohta, K. Ueda, M. Hirano, H. Hosono, *Appl. Phys. Lett.* **2004**, *85*, 1993.
- [49] Y. Kang, Y. Cho, S. Han, *Appl. Phys. Lett.* **2013**, *102*, 152104.
- [50] M. Grundmann, F.-L. Schein, M. Lorenz, T. Böntgen, J. Lenzner, H. von Wenckstern, *Phys. Status Solidi A* **2013**, *210*, 1671.